Optics & Laser Technology 42 (2010) 1103–1111

Contents lists available at ScienceDirect

Optics & Laser Technology

journal homepage: www.elsevier.com/locate/optlastec

Optical pulse compression and amplitude noise reduction using a non-linear optical loop mirror including a distributed Gires–Tournois etalon

A. González-García [a], O. Pottiez [a,*], R. Grajales-Coutiño [a], B. Ibarra-Escamilla [b], E.A. Kuzin [b]

[a] Centro de Investigaciones en Óptica (A.C.), Loma del Bosque 115, Col. Lomas del Campestre, León, Gto. 37150, Mexico
[b] Instituto Nacional de Astrofísica, Óptica y Electrónica (INAOE), Departamento de Óptica, L. Enrique Erro 1, Puebla, Pue. 72000, Mexico

ARTICLE INFO

Article history:
Received 11 August 2009
Received in revised form
25 January 2010
Accepted 1 February 2010
Available online 18 February 2010

Keywords:
Non-linear optical loop mirror
Gires–Tournois interferometer
Fibre Bragg grating

ABSTRACT

We propose and analyse numerically a novel dispersion-imbalanced non-linear optical loop mirror (NOLM) scheme allowing simultaneous compression and amplitude noise reduction of chirped ultrashort-pulsed signals. An all-fibre distributed Gires–Tournois etalon (DGTE) made of two uniform fibre Bragg gratings is inserted asymmetrically in the loop, and is used both to dispersion imbalance the NOLM and to compress the pulses. The results show that the output pulses are accompanied by side lobes, which originate from the no-uniformity of the DGTE dispersion spectrum. We analyse the formation of these side lobes and show that, in the case of highly chirped input pulses, side lobes are strongly reduced by the NOLM architecture. In this case, the device operates well even when the signal optical spectrum extends over an entire free spectral range of the DGTE. We believe that this work will be useful for the design of all-optical regeneration schemes for highly chirped data streams in optical transmission systems.

1. Introduction

The pulse broadening effect of chromatic dispersion is a major concern in optical transmission systems, as it causes the data in adjacent bit periods to overlap and produce intersymbol interference (ISI). Several techniques including the use of dispersion compensating fibre [1,2] or fibre Bragg grating [3,4] can be used to compensate the effect of dispersion in the fibre. Dispersion control is important in high-bit-rate optical transmission systems because the dispersion tolerances are reduced rapidly with increase in bit rate.

Gires–Tournois etalons (GTEs) are periodical all-pass filters that can be used to compress ultrashort optical pulses or to compensate for chromatic dispersion. The conventional GTE [5–8] consists of two plane–parallel bulk or thin-film mirrors of reflectivities $R'=1$ and $R<1$ separated by a given distance. Its group-delay spectrum exhibits resonances that are characteristic of the reflection spectrum of the Fabry–Perot interferometers. For fibre–optic applications however, it is desirable for GTEs to be made directly in the optical fibre, as it will reduce insertion loss and eliminate alignment issues. The achievement of compact all-fibre distributed Gires–Tournois etalons (DGTEs) was reported for the first time in [9], in which the bulk mirrors were replaced by fibre Bragg gratings. After this, several DGTE designs were proposed as dispersion compensation devices, which were based on chirped fibre Bragg gratings, possibly with complex apodization profiles [10,11].

The non-linear optical loop mirror (NOLM) [12] is a very versatile device that has been used extensively in applications like ultrafast switching and signal processing [13–15]. A NOLM is a Sagnac interferometer structure formed by a coupler with its output ports joined by a fibre span. Thanks to the use of the non-linear optical Kerr effect, the device presents a power-dependent transmission (switching) characteristic. Conventional devices use an asymmetry of power between the counter-propagating beams to provide switching. Such an asymmetry can be produced by an asymmetric coupler or by a loss or gain located asymmetrically in the loop.

Wong et al. [16] proposed a dispersion-imbalanced non-linear loop mirror, which is made of a 50/50 coupler and two segments of fibre; one is a standard single-mode fibre (SMF) with high anomalous dispersion and the other one is a dispersion shifted fibre (DSF) with a much lower amount of dispersion at the operating wavelength. When an input pulse enters the dispersion-imbalanced NOLM, it is split into two equal counter-propagating fields. In the clockwise (CW) propagating direction inside the loop, the incident pulse broadens quickly due to the large dispersion of the SMF and then remains broad in the DSF segment. The peak power of the broadened pulse is small and little non-linear phase shift is induced. In contrast, the counter-clockwise (CCW) pulse remains short in the DSF, which is almost dispersionless; thus the pulse acquires a large amount of non-linear phase shift. This non-linear phase shift difference is

* Corresponding author.
E-mail addresses: mscingagg@cio.mx (A. González-García), pottiez@cio.mx (O. Pottiez).

0030-3992/$ - see front matter © 2010 Elsevier Ltd. All rights reserved.
doi:10.1016/j.optlastec.2010.02.002

responsible for the intensity dependent transfer characteristic of the NOLM. In Ref. [17] the authors proposed a hybrid-type passively and actively mode locked fibre ring laser including a dispersion-imbalanced non-linear loop mirror whose operation is the same as in Ref. [16].

In this work we propose and analyse numerically a novel NOLM scheme in which a DGTE is used as a dispersion imbalance element. If the DGTE dispersion is properly adjusted, dispersion compensation and pulse compression are obtained. Simultaneously, the non-linear switching characteristic of the NOLM yields substantial amplitude noise reduction if the input peak power is properly adjusted.

2. Principle

The proposed scheme is shown in Fig. 1, where double arrows represent the state of polarisation (SOP) of the signals during their propagation in the NOLM. The interferometer includes polarisation maintaining fibre (PMF), a 3-dB polarisation maintaining (PM) fibre coupler and a polarisation beam splitter (PBS) inserted close to one of the coupler output ports. A 90° splice is realised at the other coupler output port. A linear section of standard fibre is connected at the common port of the PBS. This section includes a Faraday rotator (FR) and ends with a DGTE interferometer. Note that a fibre FR [18] can be used in order to minimise insertion losses and to preserve the all-fibre nature of the device. The signal entering the device is assumed to be linearly polarised along the *y* (vertical) axis and it is split by the 3-dB coupler into a CW beam (grey arrows in Fig. 1) and a CCW beam (white arrows). Input pulses are supposed to present a substantial linear chirp so that they are broad and have relatively low peak power. In the CCW direction, the pulses remain broad as they propagate through the loop and they are little affected by dispersion and by the Kerr-induced non-linear phase shift, due to their low peak power. A 90° splice is used to rotate the SOP of the pulses travelling in the CCW direction so that the two counter-propagating signals enter the PBS through its ordinary and extraordinary axes. At the common port of the PBS, the SOPs are orthogonal to each other and change randomly as the two signals propagate in the fibre. After rotating 45° through the FR, the signals enter the DGTE, where the chirp is compensated, so that the reflected pulses are recompressed. The incidence of the two pulse components back on the FR causes another 45° rotation of their SOP, which yield a total 90° rotation for each beam. This 90° rotation ensures that the random polarisation evolution of the beams due to fibre residual birefringence is exactly compensated after one round trip in the linear section [19]. Hence, the SOP of each beam back at the PBS common port is linear and rotated by 90° from the initial SOP. With such orientations, the beams are reintroduced through the correct PBS ports to pursue their propagation through the loop. The CCW signal reaches the coupler whereas the CW signal starts propagating in the fibre loop. As the peak power of the CW pulse was raised after compression by the DGTE, it acquires a substantial amount of non-linear phase shift. After propagation through the fibre, the CW signal polarisation is rotated by the 90° splice so that the two linearly polarised signal components arrive parallel at the coupler and successfully interfere to provide at the NOLM output port a signal of fixed linear SOP, in which the pulses are compressed and whose chirp is substantially reduced. We suppose that the input signal presents a large amount of chirp and is affected by amplitude fluctuations as well. Due to the power-dependent non-linear phase shift difference between the interfering beams, the NOLM presents a

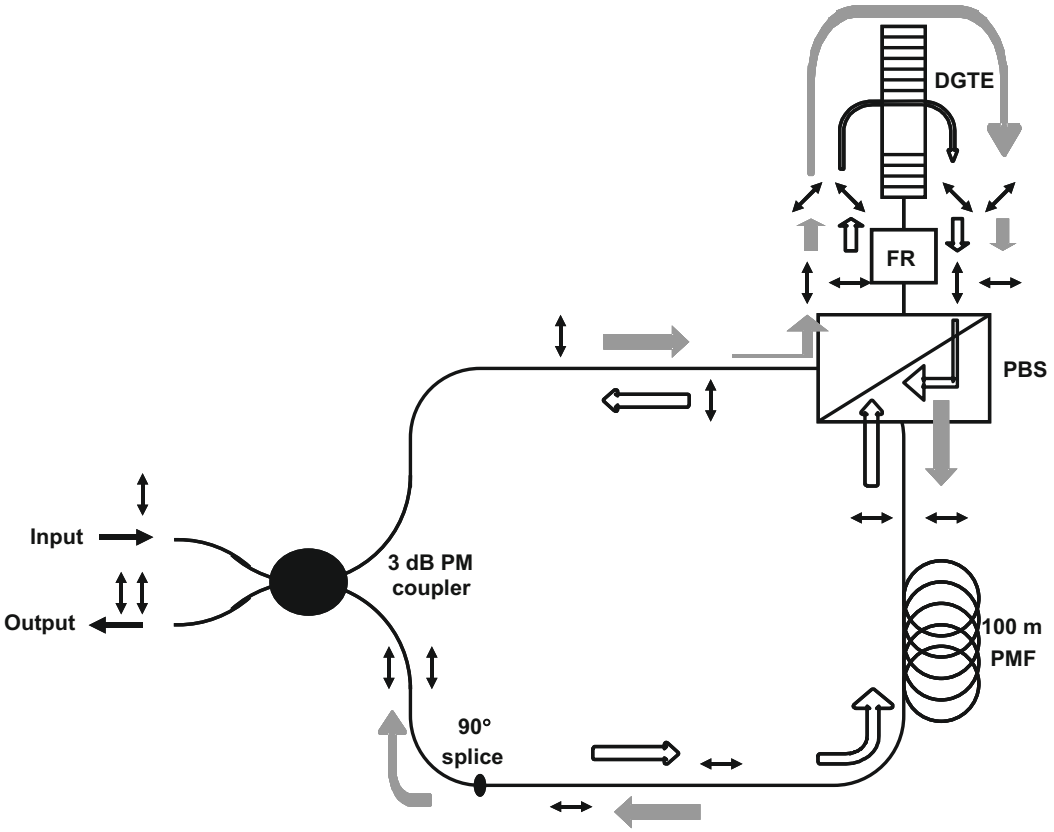

Fig. 1. Scheme of the dispersion-imbalanced NOLM scheme under study: DGTE, distributed Gires–Tournois etalon; FR, faraday rotator; PMF, polarisation maintaining fibre; and PBS, polarising beam splitter.

nearly sinusoidal switching characteristic. If the average input pulse peak power is adjusted at the maximum of the output power characteristic of the NOLM (which appears at power $\sim 1.17P_\pi$, where P_π is the transmission maximum, or switching power), then the amplitude fluctuation is also substantially reduced [14]. This configuration of the NOLM is also useful for pulse compression and pedestal suppression [13,15]. In fact when a pulse is switched by the NOLM, only its peak is transmitted while low-power components, like pedestal or noise on space bits are reflected back. As a result the NOLM can clean noise on space bits, and also further reduces the pulse duration. Note finally that this scheme preserves the SOP of the input signal and avoids the use of polarisation controllers.

3. Model

Pulse propagation in a NOLM is described by the normalised non-linear Schrödinger equation including group-velocity dispersion (GVD) and self-phase modulation (SPM). This equation writes as [20]

$$\frac{\partial u}{\partial z} + \frac{j}{2}\,\mathrm{sign}(\beta_2)\frac{\partial^2 u}{\partial t^2} = j\frac{L_D}{L_{NL}}|u|^2 u \tag{1}$$

where β_2 is the GVD parameter and sign (β_2) is the sign of β_2. The parameters z, t and u denote, respectively, the normalised distance, time and slowly varying amplitude envelope of the pulse. The normalised parameters are related to the actual parameters as follows:

$$z = Z/L_D,\ t = T/T_0,\ u = U/\sqrt{P_0},$$

where U is the envelope function of the pulse, Z is the distance along the fibre and T is the time measured in a reference frame moving at the speed of the signal. Parameter T_0 is the duration of the Gaussian pulse related to the full-width at half-maximum (FWHM) duration by $T_{FWHM} = 1.665T_0$, $L_D = T_0^2/|\beta_2|$ is the dispersion length, P_0 is the initial peak power and $L_{NL} = 1/\gamma P_0$ is the non-linear length, where γ is the Kerr coefficient. We used the split-step Fourier (SSF) method to solve Eq. (1). If now the GVD of the PMF is small, and for relatively large pulses, the effect of GVD on the pulse propagation can be neglected, and the intensity envelope of the counter-propagating pulses is nearly unaltered after propagation through the fibre. Under these conditions, the peak power values of both CW and CCW beams remain constant during propagation. Let us define the peak power enhancement factor F_p as the factor by which the CW peak power is increased after pulse compression in the DGTE. If P_{peak} is the input peak power and L_{NOLM} the PMF length, then considering the 50/50 coupling ratio, the values of non-linear phase shift at the peak accumulated by the CW and CCW beams in the PMF are $0.5F_pP_{peak}\gamma L_{NOLM}$ and $0.5P_{peak}\gamma L_{NOLM}$, respectively. Hence the non-linear phase shift difference at the peak is $0.5(F_p-1)P_{peak}\gamma L_{NOLM}$. Maximal NOLM transmission occurs at the switching power P_π, for which the non-linear phase shift difference reaches π. Its value is thus given by

$$P_\pi = 2\pi/[(F_P-1)\gamma L_{NOLM}]. \tag{2}$$

The DGTE is made of two uniform fibre Bragg gratings, and was simulated by the transfer matrix method (TMM) [21,22]. The transfer matrix of the interval d between the gratings was obtained from the phase shift $2\pi nd/\lambda$, where λ is the wavelength and n is the fibre refractive index, and the transfer matrix of each grating was obtained from the coupled-mode equations, which are

$$\frac{\partial B}{\partial Z} = j\kappa_{dc}B + j\kappa_{ac}Ae^{-j\Delta\beta Z} \tag{3}$$

$$\frac{\partial A}{\partial Z} = -j\kappa_{dc}A - j\kappa_{ac}{}^{*}Be^{j\Delta\beta Z} \tag{4}$$

where B and A are the slowly varying amplitudes for the modes propagating in the $+Z$ and $-Z$ directions, respectively, and $\Delta\beta$ is the phase mismatch. The mode coupling coefficients k_{dc} and k_{ac} are given by

$$\kappa_{dc} = n\omega\varepsilon_0\int_{-\infty}^{+\infty}\int_{-\infty}^{+\infty}\Delta n\xi\xi^{*}dxdy \tag{5}$$

$$\kappa_{ac} = n\omega\varepsilon_0\int_{-\infty}^{+\infty}\int_{-\infty}^{+\infty}v\frac{\Delta n}{2}\xi\xi^{*}dxdy = \frac{v}{2}\kappa_{dc}, \tag{6}$$

where ω is the angular frequency, ε_0 is the vacuum permittivity, Δn is the averaged refractive index perturbation introduced by the grating, v is the visibility and ξ is the modal field of the propagating modes.

4. Simulation results and discussion

The NOLM includes 100 m of PMF, with a dispersion of -2 ps/nm km at 1550 nm, and a Kerr coefficient $\gamma = 10\,\mathrm{W^{-1}km^{-1}}$. With such values of fibre length and dispersion, and for the pulse durations considered here, the pulse profile is nearly unaffected by propagation through the fibre, and only its phase is modified through the Kerr effect. Fig. 2 shows the dispersion spectrum of the DGTE formed by two uniform period gratings. The effective refractive index of the gratings is $n = 1.447$, and their spatial period is $\Lambda = 535$ nm to ensure maximal reflection at 1.55 μm. The weak grating has a length of 0.2 mm and values of Δn between 1.4×10^{-3} and 3.0×10^{-3} and $v = 1$ were used in the computational model, which results in a bandwidth of $\sim 8.3-8.4$ nm and values of reflectivity between 0.25 and 0.7 ($k_{ac} = k_{dc}/2$ between 27.5 and 60.5 $\mathrm{cm^{-1}}$); the strong grating has a length of 1 mm, $\Delta n = 2.0\times10^{-3}$ and $v = 1$, which results in a bandwidth of ~ 2.6 nm and a reflectivity of 99.9% ($k_{ac} = k_{dc}/2 = 41.5\,\mathrm{cm^{-1}}$). The separation of the gratings is 2 mm, which results in a free spectral range (FSR) of 46.8 GHz corresponding to a period of ~ 0.37 nm as shown in Figs. 2 and 3. For such values, the DGTE ring-down time is small enough to deal with pulses with durations down to ~ 10 ps. The dispersion curves are nearly periodic, and five similar channels can be found in Fig. 2. The

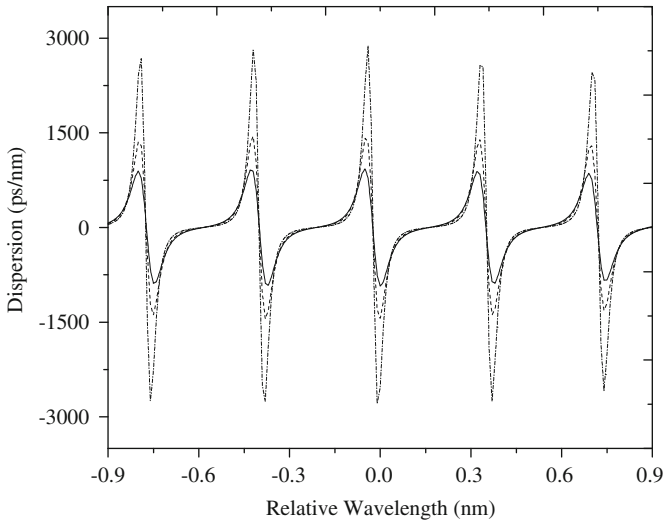

Fig. 2. Dispersion spectrum of the DGTE with amplitude of 900 ps/nm (solid line), 1400 ps/nm (dashed line) and 2800 ps/nm (dotted line) for 0.25, 0.35 and 0.5 reflectivities of the weak grating, respectively. Wavelength values relative to 1550 nm.

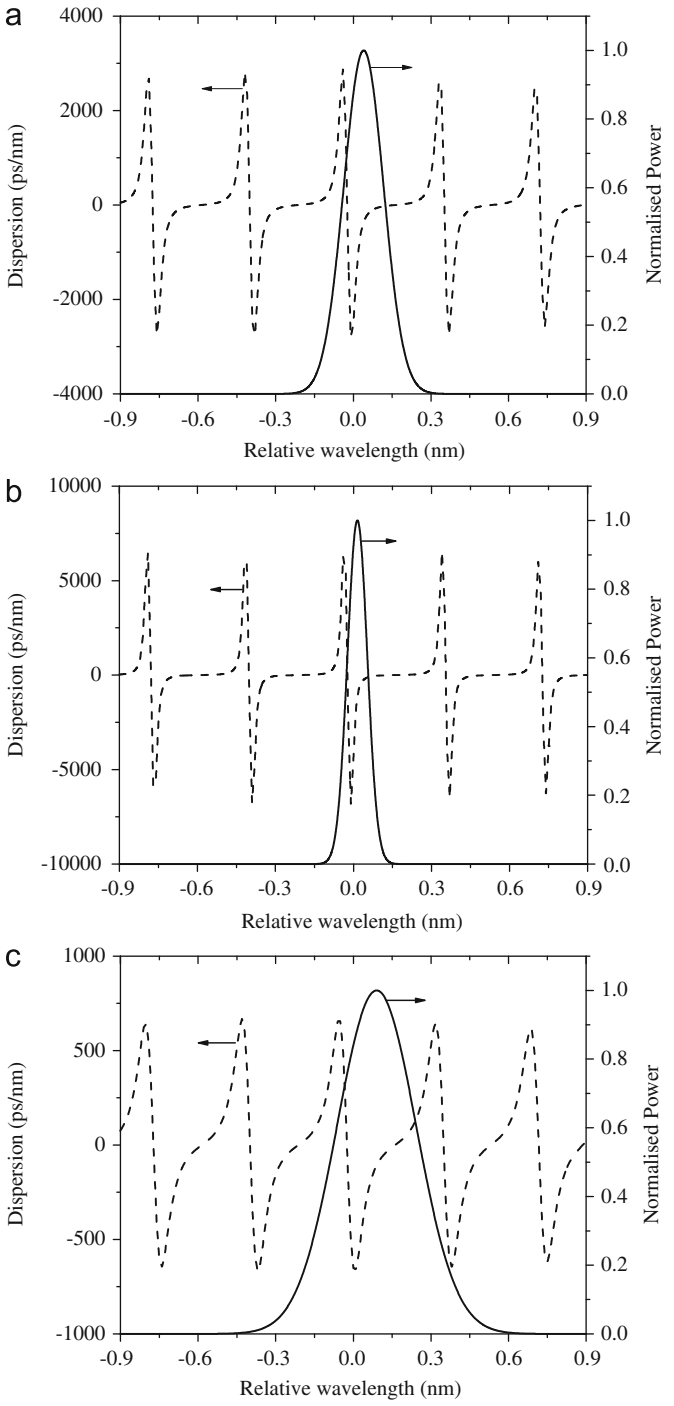

Fig. 3. Spectrum of pulses for (a) $\Delta\lambda$, (b) $\Delta\lambda/2$, and (c) $2\Delta\lambda$ FWHM spectral widths, with $\Delta\lambda = 0.18$ nm. Dispersion spectrum (dashed line) of DGTE was superimposed for comparison (the curves correspond to 0.5 (a), 0.7 (b) and 0.2 (c) reflectivities of the weak grating). Wavelength relative to 1550 nm.

curve amplitude strongly depends on the weak grating reflectivity.

We simulate the NOLM operation with linearly chirped Gaussian pulses having the same spectral width at half-maximum $\Delta\nu \approx 22.5$ GHz ($\Delta\lambda \approx 0.18$ nm) and various values of initial chirp. Initial chirp is negative, which means that the instantaneous frequency decreases linearly across the pulse from the leading to the trailing edge. In each case, the pulse spectrum is centred close to the minimum of the DGTE dispersion curve (Fig. 3(a)). By way of the weak grating reflectivity, the curve amplitude is adjusted in each case to ensure the maximum value of F_p for the CW pulse through the DGTE. The results were also improved in each case by slightly shifting to longer wavelengths the pulse spectrum from the point of minimal dispersion (by ~10–15% of the FSR). This optimal dispersion adjustment also ensures maximal pulse compression and minimal residual chirp. Table 1 presents in each case the initial chirp, the initial pulse duration at half intensity maximum T_{FWHM}, as well as the optimal dispersion at the minimum and the corresponding input peak power, compression factor and peak power enhancement factor. The peak power corresponds to the maximum of the output peak power characteristic, which ensures maximal amplitude noise reduction. Its value is usually slightly beyond the value of switching power P_π given by Eq. (2).

Table 1
Value of parameters used in the simulations for $\Delta\lambda = 0.18$ nm, and resulting input peak power, compression factor (ratio between pulse durations at the NOLM input and output) and peak power enhancement factor F_P.

Chirp	T_{FWHM} (ps)	Dispersion (ps/nm)	Input peak power (W)	Compression factor	F_p
−2	44	−900	8.2	2.8	1.7
−3	62	−1400	6.4	3.2	2.0
−4	81	−1800	5.7	3.5	2.2
−5	100	−2200	5.0	3.9	2.3
−6	119	−2800	4.7	4.2	2.4

For all the pulse parameters listed in Table 1 the initial spectral-width has the same value, which is more or less half the FSR. Fig. 4 shows the recompression results when the input peak power is adjusted at the maximum of the NOLM output power characteristic in the cases $C = -2$, -4 and -6. The figure shows that the device recompresses the pulse to a $T_{FWHM} \approx 15.6$, 23.3 and 28.0 ps at the NOLM output, respectively. These values are comparable with the 19.6 ps duration of the transform-limited pulse having the same spectrum amplitude as the input pulse (dotted lines in Fig. 4), although in reality chirp is not completely eliminated, as shown by the time-bandwidth product values $\Delta\nu_{out}T_{FWHM,out} \approx 0.93$, 0.79 and 0.70 > 0.441. This is due to the spectral widening associated with SPM, which also makes it possible that the output pulse be shorter than the transform-limited input pulse (case of $C = -2$).

Fig. 4 also shows the existence of side lobes that accompany the recompressed pulse. The magnitude of these side lobes strongly depends on the value of the initial chirp. Indeed, they are more intense for small values of initial chirp and almost disappear for chirp values from -4 to -6. The no-uniformity of the DGTE dispersion over the pulse spectrum (Fig. 3(a)) is responsible for the appearance of side lobes in the counter-propagating pulses; however these low-power components would then interfere destructively and be eliminated at the NOLM output. On the other hand, simulations show that side lobes are observed at the NOLM output even if the DGTE is replaced by a uniform dispersion spectrum. The main cause of the appearance of intense side lobes at the NOLM output is the SPM affecting the CCW pulse. Although this effect does not modify the temporal profile of the pulse through the PMF, it induces a characteristic *S*-shaped instantaneous frequency profile across the pulse [20] that adds to the initial linear profile. The CCW pulse then crosses the strongly dispersive DGTE. The newly generated red- and blue-shifted spectral components are temporally separated from the recompressed main pulse, thus increasing the side lobes. In contrast, the CW pulse does not present SPM-enhanced side lobes, as it crosses the PMF after recompression through the DGTE.

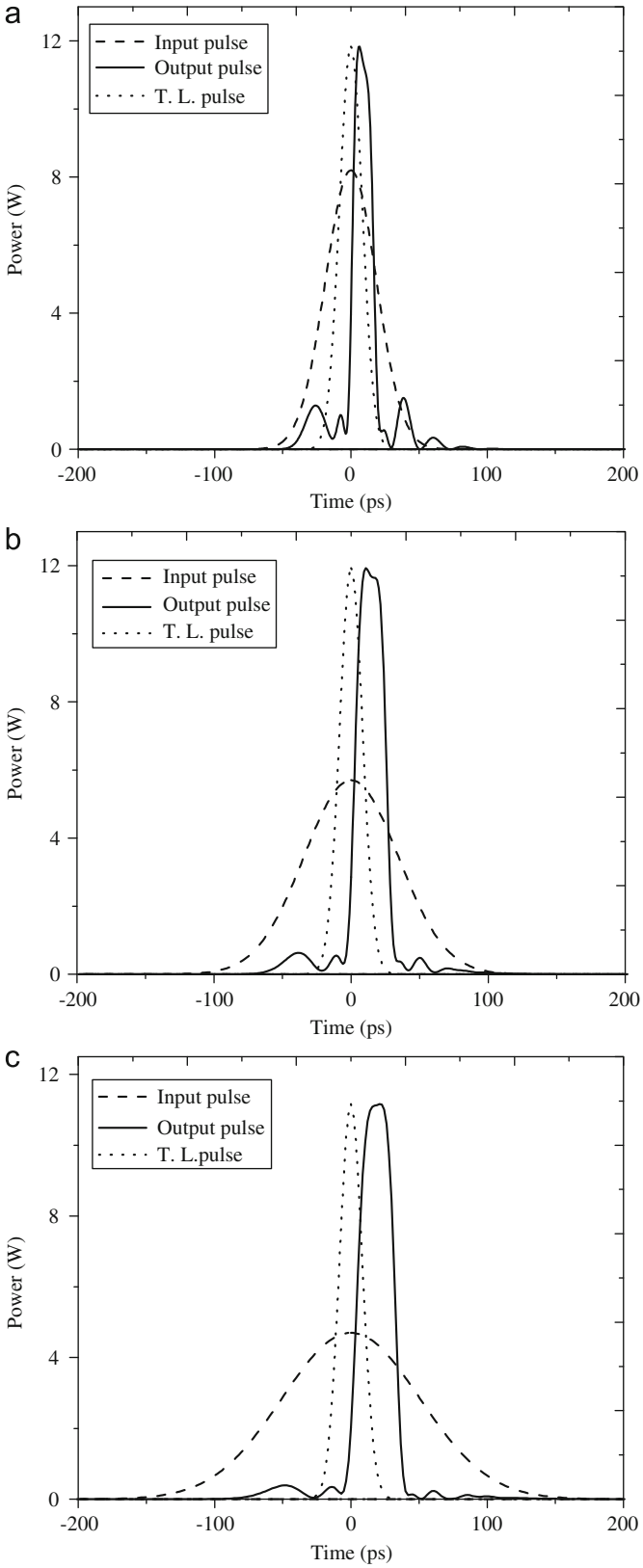

Fig. 4. Pulse power profile at the NOLM input (dashed line) and output (solid line) for (a) $C=-2$, (b) $C=-4$ and (c) $C=-6$ (all other parameters are listed in Table 1). Dotted lines show the transform-limited (TL) temporal profile of the input pulse spectrum.

In order to better understand the dependence of the side lobe intensity on initial chirp, Fig. 5 presents the CW and CCW pulse profiles after propagating through the loop, just before they recombine at the coupler, for $C=-2$ (case of Fig. 4(a)) and $C=-6$ (Fig. 4(c)). In the first case, the side lobes of the CCW pulse are much stronger than the CW pulse. This denotes a strong contribution of SPM in the formation of the CCW side lobes, due to the relatively high value of input power required for switching (see Table 1). Indeed when initial chirp is moderate, the CW pulse presents limited potential for recompression and the peak power enhancement factor F_p is small. The peak power asymmetry between CW and CCW pulses is thus small, which in turn increases the switching power (see Eq. (2)). In contrast, in the case of $C=-6$, a large compression factor and peak power enhancement are obtained for the CW pulse, which reduces the switching power. In this case, the peak power of the CCW pulse is small so that it is little affected by the SPM. The emergence of side lobes for both CW and CCW pulses is almost exclusively due to the non-uniform dispersion spectrum of the DGTE, so that they are nearly equal in amplitude, and are almost completely eliminated as they interfere destructively at the NOLM output (Fig. 4(c)).

It should also be noted in Table 1 that the compression factor is substantially higher than the power enhancement factor F_p. There are two main reasons for this. First, F_p is reduced as a consequence of the reduction in the energy of the CW pulse when it passes the DGTE, because part of this energy is transferred to side lobes. The second reason is that the non-linear transmission of the NOLM enhances the pulse compression, which is thus not exclusively due to the DGTE. Indeed, when the input peak power is adjusted near P_π, the transmission of the peak through the NOLM is nearly maximal whereas the pulse edges suffer higher loss.

As mentioned previously, the no-uniformity of the DGTE dispersion spectrum is responsible for the appearance of side lobes accompanying the recompressed CW and CCW pulses. Indeed if the pulse spectrum is in the region of negative dispersion of the DGTE, then the central spectral components undergo negative dispersion, which allows pulse compression, whereas the frequency components at the spectrum edges undergo smaller or zero values of dispersion and even positive dispersion (see Fig. 3), so that they do not regroup at the pulse centre and tend to form side lobes. One remarkable outcome of this study so far was to show that, if initial chirp is large enough (i.e., if SPM action is not significant on the CCW pulse), these side lobes are reflected by the NOLM architecture and practically disappear at the device output, and good-quality compression is observed even if the signal spectrum expands over most of the FSR of the DGTE, a range over which its dispersion varies widely and even changes sign.

One may expect, however, that the compression capabilities of the device will be limited as the signal bandwidth is increased for a given FSR. In order to analyze the effect of the signal bandwidth on the device performances, we consider a spectral width two times smaller or larger than the previously considered bandwidth ($\Delta\lambda/2$ and $2\Delta\lambda$, Fig. 3(b) and (c)). In both cases, the initial chirp $C=-4$ (as in Fig. 4(b)). In the former case (Fig. 6(a–c)), the quality of recompression is slightly better than (although comparable with) Fig. 4(b), with an output pulse duration close to the transform limit of the input pulse, F_p=2.23, and an input peak power=5.2 W for amplitude noise reduction. The side lobes are slightly lower than in Fig. 4(b) due to the slightly smaller value of input power. More dramatic changes are observed when the signal bandwidth is doubled (Fig. 6(d–f)). In this case, the pulse spectrum extends beyond one FSR, and frequency components with substantial intensity appear for zero or even positive dispersion values (Fig. 3(c)). As a consequence, a substantial portion of the energy of the CW pulse is transferred to side lobes after recompression through the DGTE (compare Figs. 6(b)

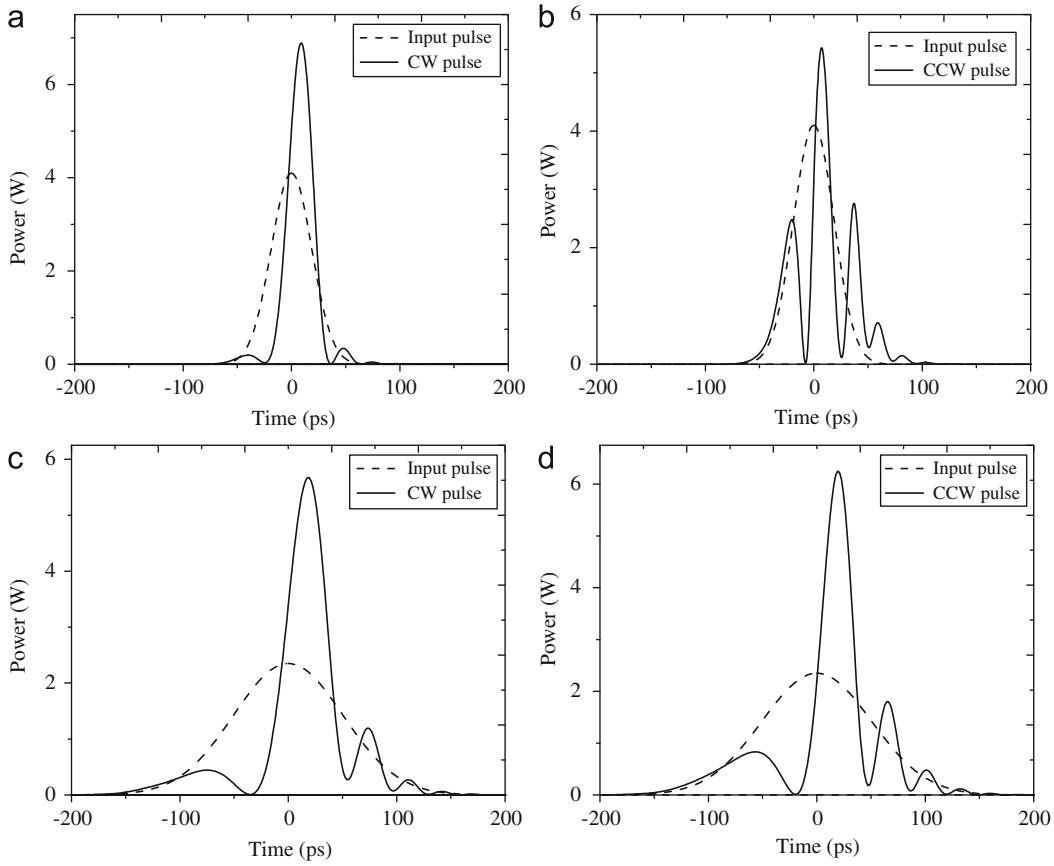

Fig. 5. CW (*a*, *c*) and CCW (*b*, *d*) pulse profiles when entering the loop (dashed) and before they recombine at the coupler (solid), for $C=-2$ (*a*, *b*) and $C=-6$ (*c*, *d*). The other parameters are listed in Table 1.

and 6(e)), and the F_p factor is severely degraded (from F_p=2.2 to 1.74), even if the pulse duration is still reduced close to the transform limit of the input signal. The F_p factor reduction causes an increase in P_π (see Eq. (2)) and in the input peak power to *7.5 W*, which in turn generates large SPM-induced side lobes in the CCW signal. Fig. 6(f) shows that these side lobes reach the intensity of the main pulse. Because of the huge asymmetry between the side lobes of the counter-propagating pulses, they do not cancel out at the NOLM output, and the output waveform presents large side lobes (Fig. 6(d)).

Fig. 7 presents the percentage of the output pulse energy included in side lobes, as a function of initial chirp, for different values of spectral width considered here: $\Delta\lambda/2$, $\Delta\lambda$ and $2\Delta\lambda$, when the DGTE dispersion was optimised in each case. In the first two cases, where the pulse spectrum remains mainly confined in one FSR, the DGTE ensures a good pulse compression with low side lobe energy for high values of initial chirp. The large value of F_p ensures a moderate switching power and thus the CCW pulse is little affected by SPM, which results in very small values of side lobes energy at the NOLM output. These values gradually increase as initial chirp is decreased, as the compression through the DGTE becomes less efficient, and smaller values of F_p yielding higher switching powers cause substantial SPM and enhanced side lobes in the CCW pulse, which are transmitted to the NOLM output. In the case of the wider spectrum, however, which extends beyond one FSR, the side lobes at the NOLM output are very large for all values of initial chirp, as a large fraction of the pulse energy facing zero or positive dispersion moves away from the main pulse through the DGTE, which induces severe F_p degradation and increase in switching power, and causes large SPM-enhanced side lobes in the CCW pulse that are transmitted to the NOLM output, quite independent of the value of the initial chirp.

To illustrate the amplitude noise reduction action of the device, Fig. 8 shows an example of eye diagram obtained at the regenerator input and output. The input signal is degraded by a substantial amount of Gaussian amplitude noise and presents intersymbol interference. The average input peak power for 1's is 4.7 W and the standard deviation of the amplitude noise is 10%, whereas the average input peak power for 0's is 0.6 W and its standard deviation is 50% as shown in Fig. 8(a). The average input peak power of 1's is adjusted to the maximum of the NOLM output power characteristic. Fig. 8(b) shows that the noise on both marks and spaces is strongly reduced at the device output. The noise standard deviation for 1's at the output is 2% for an average peak power of 11.2 W. Intersymbol interference is suppressed and the eye opening is broadened after transmission through the device. Note finally that further improvement in the pulse quality, in particular further reduction in the side lobes and pulse compression can be obtained if the signal propagates over a fibre link following the NOLM, through the interplay between anomalous dispersion and non-linear Kerr effect [23]. We thus believe that the proposed scheme may be useful both as a pre-receiver device and in the frame of in-line regeneration.

Although a large number of NOLM schemes were proposed for optical pulse shaping (compression, pedestal suppression, and amplitude equalization) or signal regeneration, in particular based on the use of an asymmetric coupler [12,13,15], attenuator [14,15] or wave retarder [24], they do not perform chirp compensation, so that a second stage should be included for

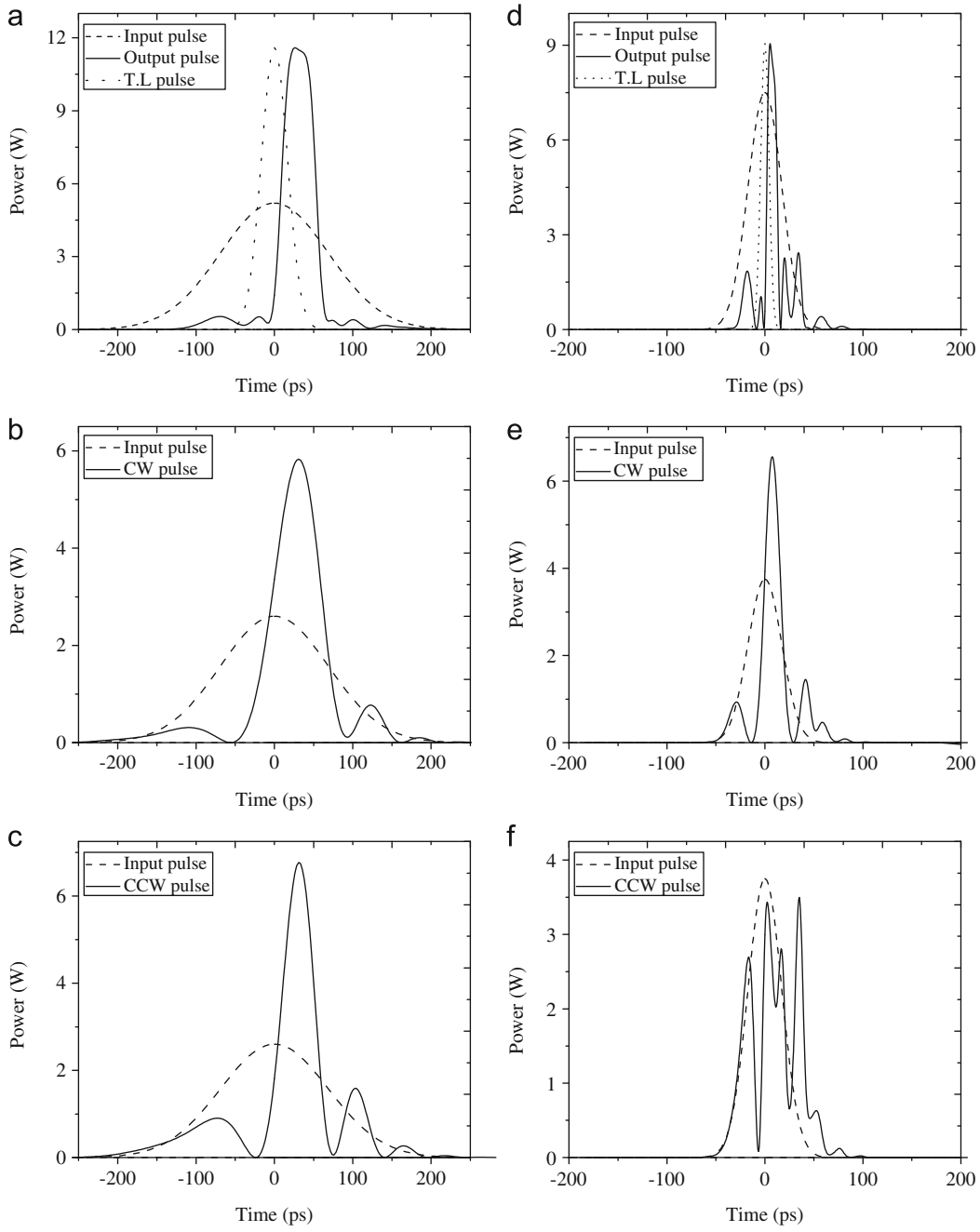

Fig. 6. The curves *a*, *b* and *c* were obtained for T_{FHWM}=162 ps, $C=-4$, $D=-6800$ ps/nm and input peak power=5.2 W, and the curves *d*, *e*, and *f* were obtained for T_{FHWM}=40.5 ps, $C=-4$, $D=-660$ ps/nm and input peak power=7.5 W; (*a*, *d*) pulse profile at NOLM input (dashed line) and output (solid line); the transform limit (TL) temporal profile of the input pulse spectrum is also shown (dotted line); (*b*, *e*) CW profile when entering the loop (dashed line) and before reaching the coupler (solid line); (*c*, *f*) CCW profile when entering the loop (dashed line) and before reaching the coupler (solid line).

complete regeneration. The dispersion-imbalanced NOLM [16], which includes two sections of fibre with different values of dispersion could be used for dispersion compensation as well; however, a large section of dispersive fibre would be needed in the loop for the regeneration of highly chirped data. In contrast, the scheme proposed in this study, including a fibre DGTE only a few millimeters long but with values of dispersion up to several thousands of ps/nm, constitutes a more compact device, which is able to perform in one stage operations such as pulse compression, pedestal suppression and amplitude equalization together with dispersion compensation, although the chirp is not completely eliminated and the pulses are accompanied by side lobes at the NOLM output.

5. Conclusion

In conclusion, we have proposed and studied through numerical simulations a novel NOLM scheme including a DGTE made of two uniform fibre Bragg gratings, for pulse compression and amplitude noise reduction of chirped ultrashort-pulsed signals. Although chirp is not completely eliminated, pulse compression down to the transform-limited duration of the input pulses is obtained at the NOLM output, for a proper choice of the DGTE dispersion. If input peak power is adjusted at the maximum of the NOLM output power characteristic, then amplitude fluctuations on marks are substantially reduced, as well as the optical power on spaces. Intersymbol interference is substantially

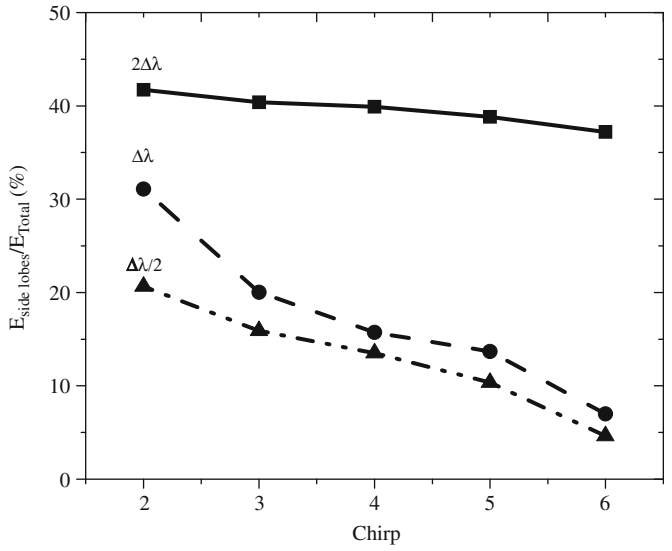

Fig. 7. Side lobes energy in function of initial chirp and spectral width; $\Delta\lambda = 0.18$ nm.

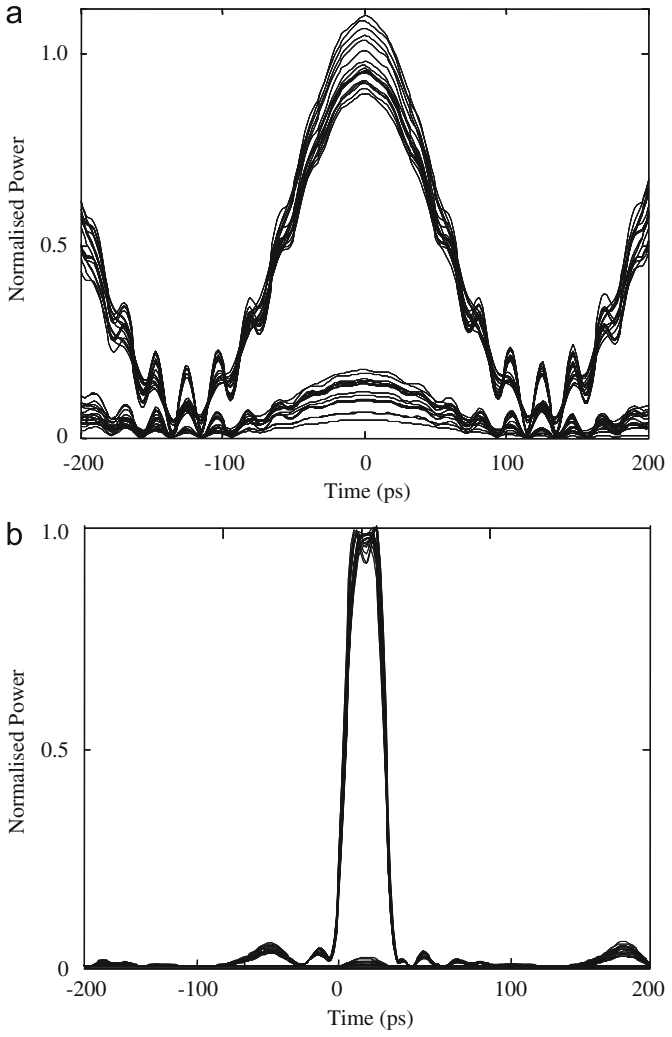

Fig. 8. Eye diagram obtained at the regenerator input (a) and output (b) for a 4 GHz data stream with Gaussian amplitude noise and average input peak power of 4.7 W. The input duration $T_{FHWM} = 119$ ps with $C = -6$, the average output peak power is 11.2 W, and the output duration is ~28 ps.

reduced as well. The compressed output pulses are also accompanied by side lobes. Side lobes appear with the counter-propagating pulses after compression through the DGTE as a consequence of large variations in the DGTE dispersion spectrum. If the initial chirp is large, however, the side lobes of CW and CCW pulses are nearly equal in amplitude, so that they are strongly reduced at the NOLM output due to destructive interference. This happens even if the pulse spectrum extends over nearly an entire FSR of the DGTE. This result is particularly interesting in practice, as it means that, with the help of a Sagnac interferometer structure, chirp compensation can be performed without the need of elaborate dispersion compensating devices presenting a uniform dispersion spectrum, like chirped and apodized fibre Bragg gratings. If the initial chirp is small, in contrast, large side lobes appear at the NOLM output, due to the SPM effect, which enhances the side lobes in the CCW direction only. Large side lobes also appear if the pulse bandwidth exceeds the FSR, so that the FSR, and thus the separation between the two fibre Bragg gratings composing the DGTE ultimately limits the device performances in terms of maximal bandwidth (or minimal transform-limited duration) of the pulses that can be regenerated. In this study, we showed that pulse compression down to ~20 ps can be obtained with an FSR of 46.8 GHz, corresponding to a grating separation of 2 mm. For shorter pulses, the FSR can be increased by further shortening the grating separation, or by overlapping gratings. We believe that this study will be useful for the development of all-optical regenerators for optical transmission systems.

Acknowledgement

A. González-García was supported by CONACyT grant 175708. O. Pottiez was supported by CONACyT grant 53990.

References

[1] Vojtech J, Karafek M, Redil J. Experimental comparison of all-optical methods of chromatic dispersion compensation in long haul transmission at speeds of 10 Gbit/s. J Opt Networking 2007;6:1340–8.
[2] Jiang Z, Yang S-D, Leaird DE, Weiner M. Fully dispersion-compensated 500 fs pulse transmission over 50 km single-mode fiber. Opt Lett 2005;30:1449–51.
[3] Ouellette F. Dispersion cancellation using linearly chirped Bragg grating filters in optical waveguides. Opt Lett 1987;12:847–9.
[4] Thibault S, Lauzon J, Cliché JF, Martin J, Duguay MA, Têtu M. Numerical analysis of the optimal length and profile of a linearly chirped fiber Bragg grating for dispersion compensation. Opt Lett 1995;20:647–9.
[5] Gires F, Tournois P. Interféromètre utilisable pour la compression d'impulsions lumineuses modulées en fréquence. C R Acad Sci Paris 1964;258:6112.
[6] Hacker M, Stobrawa G, Sauerbrey K. Femtonsecond-pulse sequence compression by Gires–Tournois interferometers. Opt Lett 2003;28:209–11.
[7] Moenster M, Griebner U, Richter W, Steinmeyer G. Resonant saturable absorber mirrors for dispersion control in ultrafast Lasers. IEEE J. Quantum Electron 2007;43:174–81.
[8] Xiu-lin W, Wen-cai H, Yu Z, Zhi-ping C. Design and analysis on a Gires–Tournois resonator based interleaver. Optoelectron Lett 2009;5:51–3.
[9] Shu X, Sugden K, Byron K. Bragg-grating-based all-fiber distributed Gires–Tournois etalons. Opt Lett 2003;28:881–3.
[10] Shu X, Sugden K, Bennion I. Dual-direction Gires–Tournois etalon based on a single complex fiber Bragg grating. Opt Lett 2006;31:2263–5.
[11] Shu X, Sugden K, Bennion I. Virtual Gires–Tournois etalons realized with phase-modulated wideband chirped fiber gratings. Opt Lett 2007;32:3546–8.
[12] Doran NJ, Wood D. Nonlinear optical loop mirror. Opt Lett 1998;13:56–8.
[13] Smith K, Doran NJ, Wigley PGJ. Pulse shaping, compression, and pedestal suppression employing a nonlinear-optical loop mirror. Opt Lett 1990;15:1294–1296.
[14] Attygalle M, Nirmalathas A, Liu HF. Novel technique for reduction of amplitude modulation of pulse strain generated by subharmonic synchronous mode-lock laser. IEEE Photon Technol Lett 2002;14:543–5.
[15] Chusseau L, Delevaque E. 250 fs optical pulse generation by simultaneous soliton compression and shaping in a nonlinear optical loop mirror including a weak attenuation. Opt Lett 1994;19:734–6.

[16] Wong WS, Namiki S, Margalit M, Haus HA, Ippen EP. Self-switching of optical pulses in dispersion-imbalanced nonlinear loop mirrors. Opt Lett 1997;22: 1150–1152.
[17] Ding Y, Wang Y, Li Z, Tan L, Liu J, Li S. Hybrid-type passively and actively modelocked fiber laser with a DI-NOLM. Chin. Opt Lett 2003;1:286–8.
[18] Annovazzi-Lodi V, Donati S, Merlo S, Leona A. All-fiber Faraday rotator made by a multiturn figure-of-eight coil with matched birefringence. J Lightwave Technol 1995;13:2349–53.
[19] Carruthers TF, Duling III IN. 10 GHz, 1.3 ps erbium fiber laser employing soliton pulse shortening. Opt Lett 1996;21:1927–9.
[20] Agrawal GP. Nonlinear Fiber Optics. San Diego: Academic press; 1995.
[21] Kashyap R. Fiber Bragg Gratings, Optics and Photonics. San Diego: Academic press; 1999.
[22] Othonos A, Kalli K. Fiber Bragg Gratings, Fundamentals and Applications in Telecommunications and Sensing. Boston: Artech House; 1999.
[23] Bello-Jimenez M, Kuzin EA, Pottiez O, Ibarra-Escamilla B, Flores-Rosas A, Duran-Sanchez M. Soliton extraction from a bunch of solitons resulting from pulse breakup by using a nonlinear optical loop mirror. J Opt Soc Am B 2009;26:1456–62.
[24] Pottiez O, Kuzin EA, Ibarra-Escamilla B, Gutierrez-Zainos F, Ruiz-Corona U, Camas-Anzueto JT. High-order amplitude regularization of an optical pulse train using a power-symmetric NOLM with adjustable contrast. IEEE Photon Technol Lett 2005;17:154–6.

Andrés González-García received the B. Eng. degree in electronics from the University of Pamplona, Colombia in 1997 and 2001 and the M. Sc. degree from Centro de Investigaciones en Óptica, León, León, Guanajuato México in 2005 and 2008, and he is currently working towards the Ph.D. degree at Centro de Investigaciones en Óptica, León, Mexico. His research interests include mode-locked fibre lasers, nonlinear optical loop mirrors and Gires–Tournois interferometers for optical signal regeneration.

Olivier Pottiez was born in 1974 in Beloeil, Belgium. He received the Electrical Engineer and Ph.D. degrees from the Faculté Polytechnique de Mons (FPMs, Mons, Belgium) in 1997 and 2001, respectively. In 2003, he realised a postdoctoral stay at Instituto Nacional de Astrofísica, Óptica y Electrónica (INAOE, Puebla, Mexico). He is currently a Researcher at Centro de Investigaciones en Óptica (CIO, León, Mexico). His present research interests include mode-locked fibre lasers for ultrashort pulse generation and fibre Sagnac interferometers for ultrafast photonics applications.

Rubén Grajales Coutiño was born in 1975 in Chiapas, Mexico. He received the Electronics Engineer degree from the Instituto Tecnologico de Tuxtla Gutierrez, Mexico, in 2002. He received the M.S. and Ph.D. degrees in optics from the Instituto Nacional de Astrofísica, Óptica y Electrónica (INAOE), Mexico, in 2004 and 2008, respectively. In 2008, he realised a postdoctoral stay at the Centro de Investigaciones en Óptica (CIO, León, México). His present research interests include mode-locked fibre lasers for ultrashort pulse generation and fibre Sagnac interferometers.

Baldemar Ibarra-Escamilla was born in Veracruz, Mexico, on April 9, 1969. He received the Bachelor degree in Electronics from the Benemérita Universidad Autónoma de Puebla. Mexico, in 1994. He received the M.S. and Ph.D. degrees in optics from the Instituto Nacional de Astrofísica, Óptica y Electrónica (INAOE), Mexico, in 1996 and 1999, respectively. During 2000, he did a postdoctoral stay at the Electro-Optics Graduate Program, University of Dayton, USA. He is currently a Researcher of the Optics Department from the INAOE. His interests are in the field of optical fibre mode-locked lasers, optical fibre amplifiers, tuneable optical fibre lasers, and fibre–optic sensors.

Evgeny A. Kuzin was born in 1948 in St. Petersburg, Russia. He graduated from the University of St. Petersburg in 1976 and obtained the Ph.D. degree from the Phys-Technical Institute of Academy of Sciences of Russia in 1983. He was affiliated with the Phys-Technical Institute from 1976 to 1995, and since 1995 he is working at the National Institute of Astrophysics, Optics and Electronics, Puebla, Mexico.